Unconventional Growth Mechanism for Monolithic Integration of III–V on Silicon

Kar Wei Ng,[†] Wai Son Ko,[†] Thai-Truong D. Tran,[†] Roger Chen,[†] Maxim V. Nazarenko,[‡] Fanglu Lu,[†] Vladimir G. Dubrovskii,[‡] Martin Kamp,[§] Alfred Forchel,[§] and Connie J. Chang-Hasnain[†,*]

[†]Department of Electrical Engineering and Computer Sciences, University of California at Berkeley, Berkeley, California 94720, United States, [‡]St. Petersburg Academic University, Khlopina 8/3, 194021 St Petersburg, Russia, and [§]Technische Physik and Wilhelm Conrad Röntgen Research Center for Complex Material Systems, University of Würzburg, Am Hubland, D97074 Würzburg, Germany

ABSTRACT The heterogeneous integration of III–V optoelectronic devices with Si electronic circuits is highly desirable because it will enable many otherwise unattainable capabilities. However, direct growth of III–V thin film on silicon substrates has been very challenging because of large mismatches in lattice constants and thermal coefficients. Furthermore, the high epitaxial growth temperature is detrimental to transistor performance. Here, we present a detailed studies on a novel growth mode which yields a catalyst-free (Al,In)GaAs nanopillar laser on a silicon substrate by metal–organic chemical vapor deposition at the low temperature of 400 °C. We study the growth and misfit stress relaxation mechanism by cutting through the center of the InGaAs/GaAs nanopillars using focused ion beam and inspecting with high-resolution transmission electron microscopy. The bulk material of the nanopillar is in pure wurtzite crystal phase, despite the 6% lattice mismatch with the substrate, with all stacking disorders well confined in the bottom-most transition region and terminated horizontally. Furthermore, InGaAs was found to be in direct contact with silicon, in agreement with the observed crystal orientation alignment and good electrical conduction across the interface. This is in sharp contrast to many III–V nanowires on silicon which are observed to stem from thin SiN_x, SiO_2, or SiO_2/Si openings. In addition, GaAs was found to grow perfectly as a shell layer on $In_{0.2}Ga_{0.8}As$ with an extraordinary thickness, which is 15 times greater than the theoretical thin-film critical thickness for a 1.5% lattice mismatch. This is attributed to the core–shell radial geometry allowing the outer layers to expand and release the strain due to lattice mismatch. The findings in this study redefine the rules for lattice-mismatched growth on heterogeneous substrates and device structure design.

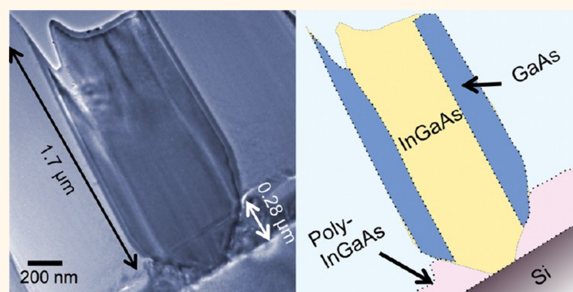

KEYWORDS: nanoneedle · nanowire · nanopillar · III–V on Si · laser · critical thickness · transmission electron microscopy

Heterogeneous integration of optoelectronic and electronic circuits is poised to transform personal electronics because it will not only enable a vast range of otherwise unattainable capabilities but also reduce power consumption, weight, and size. Although wafer bonding has resulted in successful device demonstrations, it is not readily applicable to wafers with finished CMOS circuits or silicon-based photonics consisting of diverse terrain and materials.[1] To facilitate scalable manufacturing, monolithic integration of lattice-mismatched single-crystalline materials is of paramount importance. Direct growth of III–V thin film on silicon substrates has been very challenging because of high epitaxy temperatures that are incompatible with CMOS circuits and large mismatches of lattice constants and thermal expansion coefficients between III–V compounds and silicon, causing compromises in reliability and performance.[2] As such, there has been a focus on growing three-dimensional nanostructures, which show great promise to overcome these difficulties.[3–11]

Recently, we reported a novel growth mechanism that yields catalyst-free, self-assembled, single-crystalline nanoneedles and nanopillars. The nanostructures consist of (Al,In)GaAs core–shell heterostructures and can be monolithically grown on single-crystalline silicon and sapphire at low temperature (400 °C) *via* metal–organic chemical vapor deposition (MOCVD).[3–7] We demonstrated room-temperature operation of (Al,In)GaAs light-emitting diodes and avalanche photodiodes grown on silicon substrates and

* Address correspondence to cch@eecs.berkeley.edu.

Received for review June 25, 2012 and accepted December 14, 2012.

Published online December 14, 2012
10.1021/nn3028166

© 2012 American Chemical Society

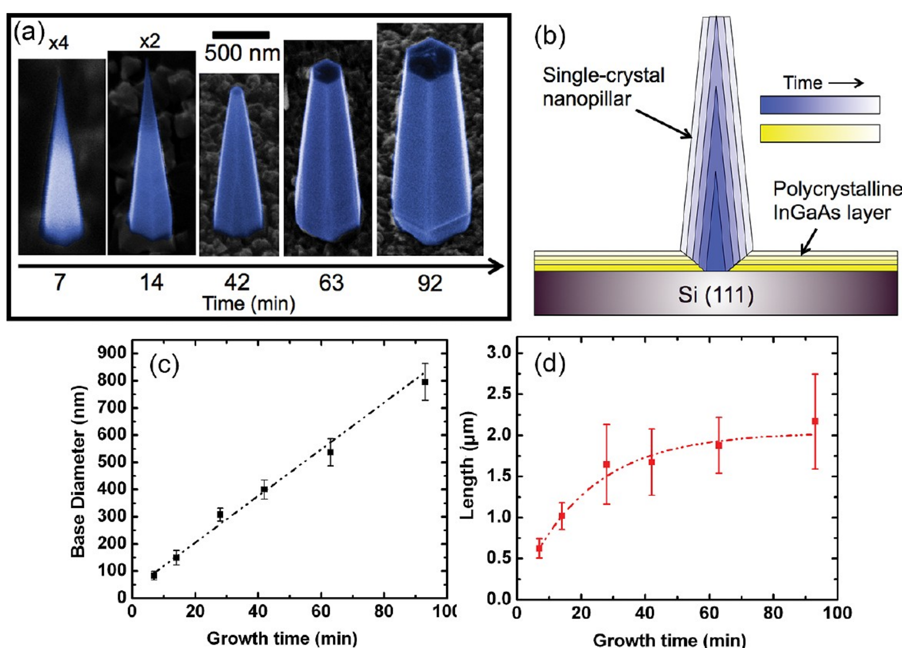

Figure 1. (a) Time evolution of the nanostructure from a sharp nanoneedle to a blunt nanopillar. (b) Schematic illustrating core–shell growth mode of the nanopillar structure. (c) Nanopillar base diameter increases linearly with time. (d) Nanopillar length scales linearly with time initially and then saturates at around 42 min of growth.

processed by standard fabrication techniques.[5] Furthermore, we reported room-temperature operation of nanopillar-based lasers on silicon by optical pulsed pumping.[6] These exciting results motivate detailed studies of this unique growth mechanism that enables high-quality growth of micrometer-sized III–V structures on silicon.

In this paper, we examine the $In_{0.2}Ga_{0.8}As$/Si interface at the nanopillar roots using high-resolution transmission electron microscopy (HRTEM) by cutting through the center of nanopillars with the use of focused ion beam (FIB). We use nanopillars with various growth duration and, hence, base diameters. Nanopillars are found to grow directly on to, and aligned with, the silicon (111) substrate. The nanopillar root above the silicon interface consists of a transition region in which stacking disorders and defects are confined within. However, above this transition region and up to their full lengths, nanopillars are shown to consist of pure, single wurtzite (WZ) phase without any misfit defects, despite a 6% lattice mismatch between $In_{0.2}Ga_{0.8}As$ and silicon. In the smallest nanopillar with a base diameter equal to 50 nm, the transition region is only 3.5 nm thick (*i.e.*, ~12 monolayers). For nanopillars with over 700 nm base diameter, the transition region is approximately 280 nm thick. The transition region assumes an inverted cone shape in the vertical direction and effectively reduces the InGaAs/silicon contact diameter to about 100 nm. Owing to the unique property of the core–shell growth mode, defects at the base do not propagate upward and only along the horizontal planes terminating at the sidewall, thus enabling high crystal quality in the bulk material above. In addition, through HRTEM, we observe that GaAs, the passivating shell layer for $In_{0.2}Ga_{0.8}As$, grows as much as 15 times larger than the critical thickness in the two-dimensional case without any misfit dislocations emerging at the interface. The nanopillar size scales with growth time and maintains excellent crystalline quality. Lasing is demonstrated under continuous wave (CW) operation when the diameter of the nanopillar base exceeds 1.5 μm. This observation signifies a new concept in heterogeneous growth and device structure design.

RESULTS AND DISCUSSION

Growth Evolution of InGaAs/GaAs Core–Shell Pillars. The evolution of the $In_{0.2}Ga_{0.8}As$/GaAs core–shell nanopillars grown on silicon is illustrated by the scanning electron microscope (SEM) images displayed in Figure 1a, which show that the nanopillar size scales with growth time. Initially, the nanostructure grows into a hexagonal pyramid with an extremely sharp tip—the facet-to-facet taper angle is as small as 5°. Growth then continues in a core–shell manner, with the sharpness well preserved. Vertical growth stops beyond a certain point (in this case after about 42 min), while radial growth continues, transforming the originally sharp needle into a hexagonal frustum. This growth mechanism is schematically illustrated in Figure 1b and is similar to that of GaAs nanoneedles grown on sapphire substrates,[7,12] with the exception of the abrupt stop to vertical growth. In Figure 1b, we also show an inverted-cone shape root as well as polycrystalline layer surrounding the pillars. The root shape was initially hypothesized based on thickness measurements of the

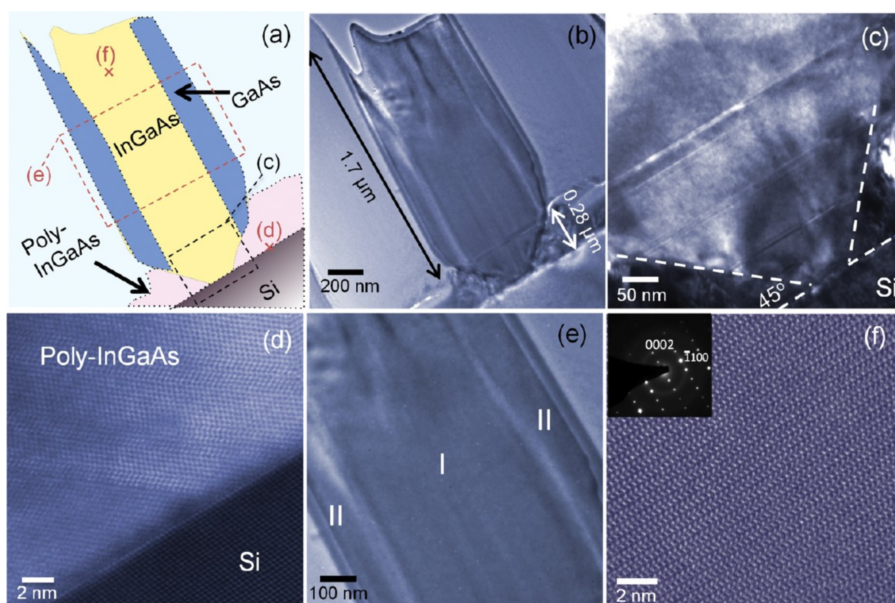

Figure 2. (a) Schematic diagram showing an InGaAs/GaAs core−shell nanopillar grown on Si, whose TEM figure is shown in (b). Areas examined in (c−f) are labeled in this schematic. (b) Cross-sectional TEM image of an InGaAs/GaAs core−shell nanopillar with a base diameter of ~740 nm. Horizontally terminated stacking faults are well confined to the bottom-most 280 nm of the tapered region. The bulk material above the tapered region consists of high-quality wurtzite phase single crystal. (c) Magnified view of the tapered root. Stacking faults arise in order to relax misfit stress. (d) Scanning transmission electron microscopy (STEM) image of polycrystalline InGaAs. Short-term crystallinity can clearly be seen. (e) Magnified view of the bulk structure. Region I: InGaAs core. Region II: GaAs shell. Neither stacking faults nor dislocations are observed. (f) HRTEM image of bulk $In_{0.2}Ga_{0.2}As$.

polycrystalline layer from cross-sectional SEM images. In this paper, we experimentally observe and verify this extraordinarily shaped tapered root for the first time.

A statistical study was performed in which more than 50 nanostructures were measured for each of the six selected growth durations. Figure 1c,d shows the average base diameter and height as a function of growth time, respectively. The base diameter increases linearly with time. In particular, the base diameter can scale up to 1.5 μm while maintaining excellent crystal quality, a distinct difference from other critical dimension-limited nanowire growth.[13−15] The average length also shows a linear dependence on time at the early stage of growth when the nanostructure is still sharp. The length saturates when the growth time reaches ~42 min, transforming the nanostructures into pillars, as shown in Figure 1d.

HRTEM Studies of InGaAs/Si Interfaces. Extensive HRTEM was carried out to investigate the origin of the nanopillar growth mechanism. Sample preparation involves the extraction of a lamella from an as-grown nanopillar on silicon (111) with the use of FIB milling and *in situ* micromanipulations.[16] We cut the nanopillars to expose $(2\bar{1}\bar{1}0)$ facets so that the distinction between WZ and zinc blende (ZB) phases can be clearly seen. Over 20 nanopillars have been examined with HRTEM in this work. Figure 2a,b shows a schematic diagram and the corresponding cross-sectional TEM image of an $In_{0.2}Ga_{0.2}As$/GaAs nanopillar growing on silicon (111), respectively. The nanopillar can be clearly seen to directly grow on silicon with a "footprint" much smaller than the base diameter of the nanopillar, which is 720 nm in this particular lamella. The footprint diameter is found to range from 70 to 130 nm. The pillar has an initial section that tapers upward with an increasing diameter at about 45°, as shown in Figure 2c. The tapered region has a thickness of 280 nm which is approximately equal to that of the surrounding layer, consisting of polytypes and defects, as seen in Figure 2c. A range of angles from about 45 to 60° were observed for various TEM samples. The formation of such an inverted cone is due to the formation of a polycrystalline layer with slower growth rate, which thus "wraps" around the bottom of the nanopillar, as illustrated in Figure 1b. We attribute the presence of the inverted cone as the key for stress relaxation in our core−shell growth mode, and this will be discussed in more detail shortly.

The polycrystalline layer surrounding the inverted cone pillar root is examined with scanning transmission electron microscopy (STEM), as shown in Figure 2d. This material is found covering the entire wafer and forms a rough, continuous layer. The STEM image shows that this material is polycrystalline with many domains, showing short-term ZB crystallinity with random orientations. The origin of this film can be attributed to the coalescence of the randomly formed ZB phase islands that nucleate during the initial growth stage at low temperature.

The bulk material of the nanopillar is pure and single-crystalline, in contrast to the defective polycrystalline layer. No defects or polytypic regimes can be

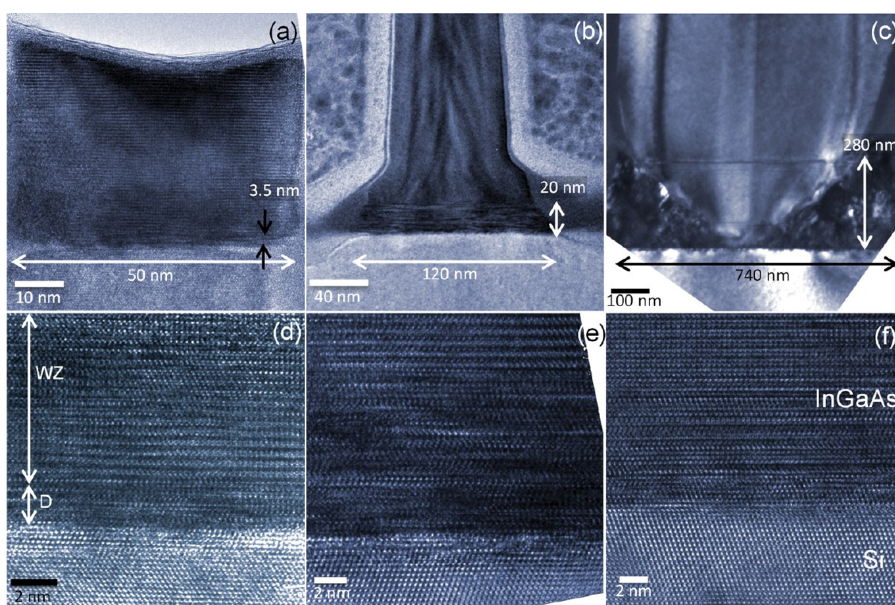

Figure 3. TEM images of InGaAs/GaAs nanopillar with base diameters of (a) 50 nm, (b) 120 nm, and (c) 740 nm. The nanostructures are free of defects except the bottom-most defective region. As base diameter increases, the thickness of the defective region increases from 3.4 to 280 nm, relaxing the 6% misfit stress between InGaAs and silicon. (d−f) Exact InGaAs/Si interfaces of nanopillars in (a−c), respectively. InGaAs stems directly on Si without any amorphous material between. In the smallest nanopillar, the defective region (labeled "D") is only 3.5 nm, or ∼12 monolayer, in thickness, as seen in (d).

observed for the length above the tapered transition region, as seen in Figure 2b,e. This indicates that most of the stress is relieved in the bottom transition region and that the crystal above is essentially stress-free. In this particular TEM sample, the single-crystal bulk material extends 1.7 μm above the root and would continue all the way up to the tip of the nanopillar. Figure 2f shows a HRTEM image of $In_{0.2}Ga_{0.2}As$ in the bulk along [1$\bar{2}$10]. The lattice displays a characteristic zigzag configuration, attesting to the WZ nature of the crystal. Excellent crystal quality is confirmed by the very clear diffraction pattern taken along [1$\bar{2}$10] in the inset of Figure 2f.

Stacking disorders and defects are found in the nanopillar bottom-most transition region, as seen in Figure 2c. These defects terminated horizontally and do not propagate vertically. This and the inverted tapering are the key to the high-quality growth of the nanopillars. Figure 3a−c shows the roots of nanopillars with different growth time and, hence, base diameters. As mentioned before, the footprint of InGaAs on silicon is typically 70−130 nm, which is likely to be the average distance between islands during initial nucleation. When the nanopillar size is less than 130 nm, the surrounding polycrystalline grains are yet to get close enough and mask the nanopillar growth. Therefore, an inverted cone is not observed in Figure 3a,b. Nevertheless, the same phenomenon is observed in all three cases—all stacking faults and defects are well confined within the bottom-most region. In particular, when the base diameter is 50 nm, stacking defects only extend 3.5 nm, or ∼12 monolayers, above silicon, as seen in Figure 3a,d. As nanopillar base diameter increases, the disordered region gets thicker to accommodate the extra misfit stress, as seen in Figure 3b,c. We note that all defects propagate laterally rather than vertically along [0001]. In other WZ crystals like GaN, threading dislocations propagating along the growth direction are usually observed. Epitaxial lateral overgrowth (ELOG) is then developed to promote lateral growth so as to bend the dislocations from propagating upward into the active region.[17] The growth mechanism described here, on the other hand, is a pure core−shell growth mode in which growth occurs only in the lateral direction, except the very tip of the structure. Misfit defects therefore propagate horizontally and terminate at the sidewall. Hence, the crystal structure remote from the substrate stabilizes into a single pure WZ phase, which is energetically preferred due to a lower number of dangling bonds on the WZ sidewalls.[24] In addition to stacking disorders, inverted tapering is crucial in stress relaxation. The inverted-cone taper serves to limit the footprint area while the base expands, somewhat similar to the critical diameter observed in nanowires below which misfit strain can be relaxed elastically.[13−15] Although the footprint (>70 nm) has already exceeded the theoretical critical value, small contact area and outward tapering still facilitate elastic strain relaxation. As seen in Figure 3c, stacking disorders only appear infrequently in the tapered transition region, suggesting that the special taper geometry is the dominant mechanism in stress relaxation.

To realize electrical devices, it is essential to study how the III−V material is connected to the substrate

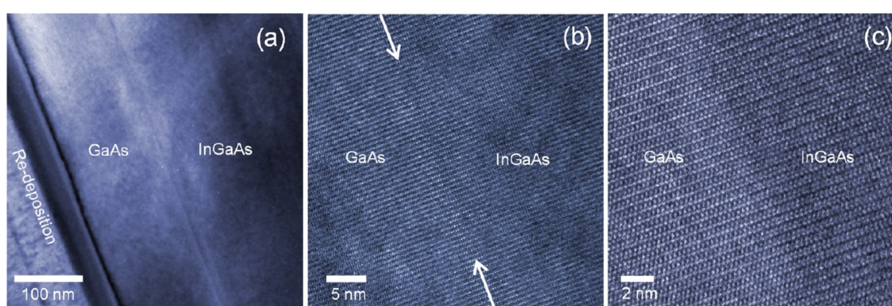

Figure 4. (a) GaAs shell (150 nm) grown seamlessly on $In_{0.2}Ga_{0.8}As$ with no defects emerging at the interface. (b) Higher magnification of the interface. (c) HRTEM image of the interface. The high-quality WZ structure continues seamlessly from InGaAs to GaAs.

nanoscopically. Figure 3d–f shows the HRTEM images of the exact InGaAs/Si interfaces of the nanopillars shown in Figure 3a–c, respectively. We note that InGaAs always grows directly on silicon without any amorphous material between. This is in sharp contrast to many III–V nanowires on silicon, which are observed to stem from thin SiN_x, SiO_2, or SiO_2/Si openings.[18–20] While direct electrical conduction from III–V to silicon is guaranteed, III–V stacking disorders at the root may seem to be a hindrance to excellent electrical performance. However, remarkable diode behavior can still be obtained in the presence of stacking disorders. In particular, the *I*–*V* curves obtained from the nanopillar photodetector we reported recently show an ideality factor close to 2,[21] which is a typical value for a high-quality double heterostructure p–n junction with radiative recombination. We attribute this to the fact that the junction is well embedded in the single-crystalline bulk material and thus the effect of defects is insignificant. This explains the excellent electrical properties observed in the nanopillar devices in our previous work.[5]

In addition to the stress relaxing mechanism, it is also important to understand how nanopillars nucleate. We believe that InGaAs initially nucleates as islands with various orientations in both WZ and ZB phases, as observed in Figure 2d and SEM studies (not shown here). This is in contrast to conventional III–V epitaxial growth in which ZB is the dominant crystal phase. The main reason for such discrepancy is that our growth temperature is substantially lower than conventional growth. Adatoms possess lower kinetic energy on average such that they can get incorporated into the lattice before migrating to the most energetically favorable ZB lattice sites. Probabilistically, adatoms settle down at the WZ lattice sites, resulting in the formation of WZ phase crystal seeds. This phenomenon is actually observed in the growth of GaP on silicon under kinetically driven conditions,[22] confirming the possibility that ZB and WZ crystal seeds can coexist at the nucleation phase. The probabilistic nature of WZ crystal formation can be observed from the random distribution of InGaAs nanopillars, which is similar to the growth of GaAs nanoneedles on silicon.[4] WZ crystal stabilizes as a metastable phase (*i.e.*, a local energy minimum in addition to the global energy minimum at ZB phase) and growth continues. We note that the low growth temperature and V/III environment favor the coherent growth of WZ phase over ZB phase crystal. This can be observed from the vertical growth rate of wurtzite nanostructure being over 10 times faster than that of polycrystalline ZB InGaAs. As a result, although both WZ and ZB islands nucleate directly on silicon at the same time, WZ seeds enlarge coherently in a core–shell fashion and become single-crystalline nanopillar while randomly oriented ZB islands coalesce and evolve into a polycrystalline layer.

High-Quality Mismatched Growth of GaAs on $In_{0.2}Ga_{0.8}As$ beyond Critical Thickness. The core–shell nanopillar growth facilitates thicker growth of lattice-mismatched layers, which is of critical importance for heterojunction device engineering. Previously, the thin-film critical thickness of $In_{0.2}Ga_{0.8}As$ on GaAs(100) was found to be less than 10 nm (~1.5% lattice mismatch).[23] Given the unique core–shell growth mode and pure WZ phase, it is important to explore if a similar critical thickness exists. A series of samples with various GaAs thicknesses were grown on $In_{0.2}Ga_{0.8}As$ cores, while keeping the same core diameter of 600 nm and growth conditions. No defects were observed for GaAs grown on $In_{0.2}Ga_{0.8}As$ pillars up to a thickness of 150 nm, as shown in Figure 4a. HRTEM images in Figure 4b,c show that GaAs continues seamlessly on $In_{0.2}Ga_{0.8}As$, maintaining the characteristic zigzag WZ lattice arrangement. In over 20 lamellas examined, no observable misfit defects were found along the entire interface in the bulk of the nanostructure. This limit-breaking coherent growth comes as a consequence of the core–shell growth mode, where the surface area of the shell layer increases almost linearly with its thickness. A large surface area facilitates the elastic relaxation of stress induced at the $In_{0.2}Ga_{0.8}As$/GaAs interface.[24] This unique stress relaxation mechanism enables the growth of mismatched layers to thicknesses far beyond the conventional thin-film limit and could lead to device structures with potentially unprecedented functionalities.

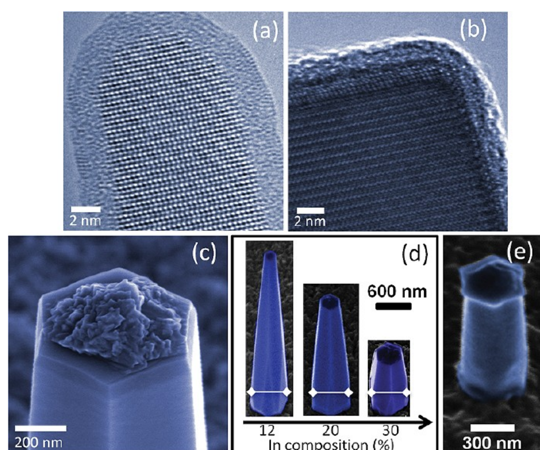

Figure 5. (a) HRTEM image of a sharp InGaAs/GaAs nanoneedle. The entire tip is in pure WZ phase. (b) HRTEM image of a blunt pillar. The topmost few monolayers are in ZB phase, ceasing vertical growth of the nanostructure. (c) Tip of a nanopillar with polycrystalline InGaAs layer growing on top. (d) Nanopillars with different indium compositions. Nanopillar length decreases as In% increases. (e) Nanopillar after citric acid etch. The etch rate difference suggests that indium composition is higher at the tip.

Vertical Growth Termination and Phase Transition Due to Indium Incorporation. The nanoneedles transform into a pillar shape after certain growth time, as shown in Figure 1. We investigate the origin of the vertical growth termination by examining the tips of sharp and blunt InGaAs/GaAs nanostructures with HRTEM, depicted in Figure 5a,b, respectively. Sample preparation was done by simple wipe-down of the as-grown nanostructures onto a TEM copper grid. Sharp nanoneedle possesses a pure WZ structure which extends all the way up to the topmost layer, as seen in Figure 5a. On the other hand, the blunt nanopillar has ZB monolayers sitting on top of pure WZ phase body as the terminating layers, shown in Figure 5b. As mentioned previously, the growth of ZB InGaAs is unfavorable under the growth conditions used in this work. Upon formation of the ZB crystal, the growth rate at the tip reduces significantly. In some extreme cases, the ZB crystal at the tip evolves into a polycrystalline cluster, similar to the ZB InGaAs layer surrounding the nanopillar, as seen in Figure 5c. This implies that a sudden phase switch at the tip effectively stops the core−shell growth in the vertical direction. This is not observed in the binary GaAs nanoneedle grown in the same condition. A series of InGaAs nanostructures with different indium compositions were then grown to study the impact of indium on vertical growth termination, as shown in Figure 5d. We note that the three samples have nearly the same diameters, as illustrated by the white arrows in the figure. Nanopillar length, however, decreases significantly with indium composition. The higher the indium flow, the earlier the onset of truncation. We attribute the truncation to the different diffusion lengths of indium and gallium. Since indium can diffuse over a longer distance, the tip of the nanostructure has a higher supply of indium than gallium, resulting in a gradual increase in indium composition. This increase in indium triggers phase transition from WZ to ZB at the tip, thus frustrating the characteristic core−shell growth in the vertical direction. On average, nanopillars can reach a length of between 1.7 and 2 μm.

To verify that indium composition is indeed larger at the tip, we etched the InGaAs/GaAs nanopillars with 5:1 citric acid/peroxide (30%). Figure 5e shows a 30° tilt view of a typical nanopillar after a 16 min etch. The body of the pillar is severely etched such that the hexagonal facets have completely disappeared. The tip of the pillar, however, remains hexagonal in shape and has a bigger diameter than the bulk. This shows that the etch rate at the tip is much lower than in the bulk of the nanopillar. It has been reported elsewhere that the etch rate of citric acid falls with increasing indium composition in InGaAs.[25] Such an etch rate difference observed in Figure 5e attests to the fact that indium accumulation does occur at the tip of the nanopillar.

Continuous Wave Operation of InGaAs Nanolaser. Excellent crystal quality gives rise to remarkable optical properties. CW operation is achieved in nanopillar lasers grown on silicon under optical pumping at 4 K. A 785 nm diode laser was used as the CW pumping source. Figure 6a shows the emission spectra under various pump powers. At low pump levels, spontaneous emission is observed with a peak wavelength at 970 nm and a 3 dB bandwidth of approximately 17 nm. As the excitation power increases, we observe the emergence of a cavity mode at 960 nm, which finally evolves into laser oscillation. Clear threshold behavior in the pump power dependence of light output power and the near-field pattern are illustrated in the inset of Figure 6b. Lasing action is also indicated by the prominent line width narrowing, as seen in Figure 6c. At a pump power of 1000 μW, the laser line width is as narrow as 0.2 nm, which is comparable with the narrowest line widths observed for existing nanocavity lasers.[6,26−29] The laser assumes a helically propagating mode,[6] and hence, the output emitted from the top surface is relatively low. Nevertheless, more than 5.5 μW of CW optical power was collected, which is among the highest reported for nanolasers. This underscores the potential usefulness of integrating these nanopillar lasers onto silicon for various applications.

Compared to conventional nanowire work, a major advantage of this growth process is that it enables high-quality submicrometer growth of III−V on silicon, as attested by detailed HRTEM studies. The bulk of the structure is in pure wurtzite phase, which is in contrast to most nanowires reported with zinc blende/wurtzite polytypism. As our nanostructure can scale up to micrometer size, lasing from a *single, as-grown* pillar

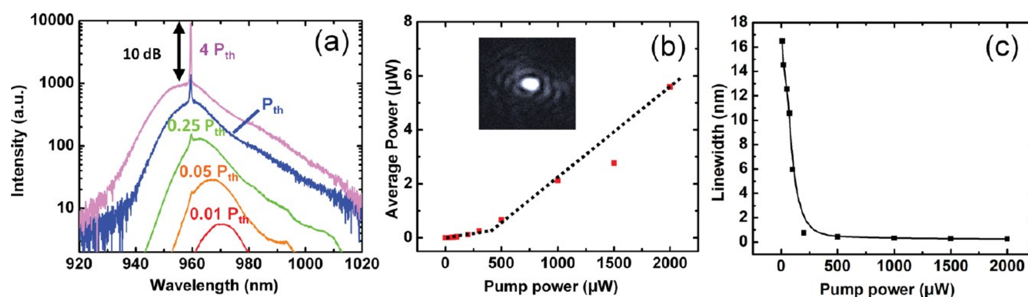

Figure 6. (a) CW emission spectra at different pump powers. The cavity mode peak is observed when the pump power is as low as 0.25 times the threshold pump power (0.25 P_{th}). A sideband suppression ratio of 10 dB is observed at 4 P_{th}. (b) Emission power plotted as a function of pump power. Threshold behavior is observed, and the maximum output power is close to 6 μW. The inset shows clear speckle patterns in the near-field. (c) Line width narrowing is observed with increasing pump power. The line width reduces by a factor of ∼80 near and above the laser threshold.

can be achieved. This is yet to be demonstrated in other nanowire work because insufficient optical feedback can be provided by the small-sized cavity. With InGaAs/GaAs core−shell nanopillars, we obtained a density of around 1 per 200 μm^2, similar to that of GaAs nanoneedles grown on silicon reported in our previous work.[4] Since each pillar is large enough, it will be processed and used as a single device, as evident by the optically pumped laser reported here. Hence, different from nanowires, where an ensemble would be required to function as a laser,[30] high density may be neither necessary nor desirable. We note that this growth has been repeated over 500 times, and this signifies the potential of this work as an important pathway for heterogeneous integration.

CONCLUSIONS

We studied the growth mechanism for a new nanocrystal growth mode on a lattice-mismatched substrate. InGaAs was found to grow directly on silicon without any amorphous layer between. Misfit strain between silicon and InGaAs is relaxed *via* an interesting inverted-cone shape tapering of the root, in which horizontally terminated stacking disorders are confined. Moreover, the special geometry, which arises during core−shell growth, facilitates elastic stress relaxation at the $In_{0.2}Ga_{0.8}As$/GaAs interface, resulting in a GaAs thickness exceeding 15 times the thin-film critical thickness. This study opens a new chapter in the heterogeneous integration of lattice-mismatched materials and their device structure design.

METHODS

Sample preparation prior to the metal−organic chemical vapor deposition (MOCVD) growth involves standard solvent cleaning and mechanical roughening of the substrate surface, similar to 3−7. The solvents include acetone and methanol to remove organic contaminants, followed by surface deoxidation by buffered oxide etchant. InGaAs/GaAs core−shell nanopillars are grown at 400 °C, with a V/III ratio ranging from 42 to 48 under a pressure of 76 Torr.

Conflict of Interest: The authors declare no competing financial interest.

Acknowledgment. This work was supported by the MARCO Interconnect Focus Center and the Department of Defense National Security Science and Engineering Faculty Fellowship, and a Research Award of the von Humboldt Foundation. We thank the National Center of Electron Microscopy for the use of their facilities.

REFERENCES AND NOTES

1. Fang, A. W.; Park, H.; Cohen, O.; Jones, R.; Paniccia, M. J.; Bowers, J. E. Electrically Pumped Hybrid AlGaInAs−Silicon Evanescent Laser. *Opt. Express* **2006**, *14*, 9203–9210.
2. Olsson, F.; Xie, M.; Lourdudoss, S.; Prieto, I.; Postigo, P. A. Epitaxial Lateral Overgrowth of InP on Si From Nano-Openings: Theoretical and Experimental Indication for Defect Filtering Throughout the Grown Layer. *J. Appl. Phys.* **2008**, *104*, 093112.
3. Moewe, M.; Chuang, L. C.; Dubrovskii, V. G.; Chang-Hasnain, C. J. Growth Mechanisms and Crystallographic Structure of InP Nanowires on Lattice-Mismatched Substrates. *J. Appl. Phys.* **2008**, *104*, 044313-4.
4. Moewe, M.; Chuang, L. C.; Crankshaw, S.; Ng, K. W.; Chang-Hasnain, C. J. Core−Shell InGaAs/GaAs Quantum Well Nanoneedles Grown on Silicon with Silicon-Transparent Emission. *Opt. Express* **2009**, *17*, 7831–7836.
5. Chuang, L. C.; Sedgwick, F. G.; Chen, R.; Ko, W. S.; Moewe, M.; Ng, K. W.; Tran, T. T. D.; Chang-Hasnain, C. J. GaAs-Based Nanoneedle Light Emitting Diode and Avalanche Photodiode Monolithically Integrated on a Silicon Substrate. *Nano Lett.* **2011**, *11*, 385–390.
6. Chen, R.; Tran, T. T. D.; Ng, K. W.; Ko, W. S.; Chuang, L. C.; Sedgwick, F. G.; Chang-Hasnain, C. J. Nanolasers Grown on Silicon. *Nat. Photonics* **2011**, *5*, 170–175.
7. Chuang, L. C.; Moewe, M.; Ng, K. W.; Tran, T. T. D.; Crankshaw, S.; Chen, R.; Ko, W. S.; Chang-Hasnain, C. J. GaAs Nanoneedles Grown on Sapphire. *Appl. Phys. Lett.* **2011**, *98*, 123101.
8. Duan, X.; Huang, Y.; Agarwal, R.; Lieber, C. M. Single-Nanowire Electrically Driven Lasers. *Nature* **2003**, *421*, 241–245.
9. Mårtensson, T.; Svensson, C. P. T.; Wacaser, B. A.; Larsson, M. W.; Seifert, W.; Deppert, K.; Gustafsson, A.; Wallenberg, L. R.; Samuelson, L. Epitaxial III−V Nanowires on Silicon. *Nano Lett.* **2004**, *4*, 1987–1990.
10. Lai, E.; Kim, W.; Yang, P. Vertical Nanowire Array-Based Light Emitting Diodes. *Nano Res.* **2008**, *1*, 123–128.
11. Sun, K.; Jing, Y.; Park, N.; Li, C.; Bando, Y.; Wang, D. Solution Synthesis of Large-Scale, High-Sensitivity ZnO/Si Hierarchical

Nanoheterostructure Photodetectors. *J. Am. Chem. Soc.* **2010**, *132*, 15465–1546.
12. Dubrovskii, V. G.; Nazarenko, M. V.; Chuang, L. C.; Ko, W. S.; Ng, K. W.; Chang-Hasnain, C. J. Growth Kinetics of GaAs Nanoneedles on Silicon and Sapphire Substrates. *Appl. Phys. Lett.* **2011**, *98*, 153113.
13. Chuang, L. C.; Moewe, M.; Chase, C.; Kobayashi, N. P.; Chang-Hasnain, C. J.; Crankshaw, S. Critical Diameter for III−V Nanowires Grown on Lattice-Mismatched Substrates. *Appl. Phys. Lett.* **2007**, *90*, 043115.
14. Cirlin, G. E.; Dubrovskii, V. G.; Soshnikov, I. P.; Sibirev, N. V.; Samsonenko, Y. B.; Bouravleuv, A. D.; Harmand, J. C.; Glas, F. Critical Diameters and Temperature Domains for MBE Growth of III−V Nanowires on Lattice Mismatched Substrates. *Phys. Status Solidi RRL* **2009**, *3*, 112–114.
15. Ertekin, E.; Greaney, P. A.; Chrzan, D. C.; Sands, T. D. Equilibrium Limits of Coherency in Strained Nanowire Heterostructures. *J. Appl. Phys.* **2005**, *97*, 114325.
16. Huang, Z. Combining Ar Ion Milling with FIB Lift-Out Techniques To Prepare High Quality Site-Specific TEM Samples. *J. Microsc.* **2004**, *215*, 219–223.
17. Hiramatsu, K.; Nishiyama, K.; Motogaito, A.; Miyake, H.; Iyechika, Y.; Maeda, T. Recent Progress in Selective Area Growth and Epitaxial Lateral Overgrowth of III-Nitrides: Effects of Reactor Pressure in MOVPE Growth. *Phys. Status Solidi A* **1999**, *176*, 535–543.
18. Guo, W.; Zhang, M.; Bhattacharya, P.; Heo, J. Auger Recombination in III-Nitride Nanowires and Its Effect on Nanowire Light-Emitting Diode Characteristics. *Nano Lett.* **2011**, *11*, 1434–1438.
19. Koblmüller, G.; Hertenberger, S.; Vizbaras, K.; Bichler, M.; Bao, F.; Zhang, J. P.; Abstreiter, G. Self-Induced Growth of Vertical Free-Standing InAs Nanowires on Si(111) by Molecular Beam Epitaxy. *Nanotechnology* **2010**, *21*, 365602.
20. Morral, A. F. i; Colombo, C.; Arbiol, J.; Morante, J. R.; Abstreiter, G. Nucleation Mechanism of Gallium-Assisted Molecular Beam Epitaxy Growth of Gallium Arsenide Nanowires. *Appl. Phys. Lett.* **2008**, *92*, 063112.
21. Chen, R.; Parekh, D.; Ng, K. W.; Chang-Hasnain, C. J. High-Speed Avalanche Photodiodes Using III-V Nanopillars Monolithically Grown on Silicon. *Group IV Photonics (GFP), 2012 IEEE 9th International Conference* **2012**, 48−50.
22. Narayanan, V.; Mahajan, S. Orientation Mediated Self-Assembled Gallium Phosphide Islands Grown On Silicon. *Philos. Mag. A* **2000**, *80*, 555–572.
23. Zou, J.; Cockayne, D. J. H.; Usher, B. F. Misfit Dislocations and Critical Thickness in InGaAs/GaAs Heterostructure Systems. *J. Appl. Phys.* **1993**, *73*, 619–626.
24. Nazarenko, M. V.; Sibirev, N. V.; Ng, K. W.; Ren, F.; Ko, W. S.; Dubrovskii, V. G.; Chang-Hasnain, C. J. Elastic Energy and Critical Thickness for Plastic Deformation in the Core−Shell InGaAs/GaAs Nanopillars. To be submitted.
25. DeSalvo, G. C.; Tseng, W. F.; Comas, J. Etch Rates and Selectivities of Citric Acid/Hydrogen Peroxide on GaAs, $Al_{0.3}Ga_{0.7}As$, $In_{0.2}Ga_{0.8}As$, $In_{0.53}Ga_{0.47}As$, $In_{0.52}Al_{0.48}As$, and InP. *J. Electrochem. Soc.* **1992**, *139*, 831–835.
26. Yu, K.; Lakhani, A.; Wu, M. C. Subwavelength Metal−Optic Semiconductor Nanopatch Lasers. *Opt. Express* **2010**, *18*, 8790–8799.
27. Hill, M. T.; Oei, Y. S.; Smalbrugge, B.; Zhu, Y.; Vries, T.; Veldhoven, P. J.; Otten, F. W. M.; Eijkemans, T. J.; Turkiewicz, J. P.; Waardt, H.; Geluk, E. J.; Kwon, S. H.; Lee, Y. H.; Nötzel, R.; Smit, M. K. Lasing in Metallic-Coated Nanocavities. *Nat. Photonics* **2007**, *1*, 589–594.
28. Lu, C. Y.; Chang, S. W.; Chuang, S. L.; Germann, T. D.; Bimberg, D. Metal-Cavity Surface-Emitting Microlaser at Room Temperature. *Appl. Phys. Lett.* **2010**, *96*, 251101.
29. Lee, J. H.; Khajavikhan, M.; Simic, A.; Gu, Q.; Bondarenko, O.; Slutsky, B.; Nezhad, M. P.; Fainman, Y. Electrically Pumped Sub-wavelength Metallo-Dielectric Pedestal Pillar Lasers. *Opt. Express* **2011**, *19*, 21524–21531.
30. Scofield, A.; Kim, S. H.; Shapiro, J. N.; Lin, A.; Liang, B. L.; Scherer, A.; Huffaker, D. L. Room Temperature Continuous Wave Lasing in Nanopillar Photonic Crystal Cavities. *Conference on Lasers and Electro-Optics (CLEO)* **2012**, CTh4M.